

Time-dependent Mandel Q parameter analysis for a hexagonal boron nitride single photon source: supplement

CALLUM JONES,^{1,*}  JOLLY XAVIER,^{1,2} SAMIR VARTABI KASHANIAN,¹ MINH NGUYEN,³ IGOR AHARONOVICH,^{3,4} AND FRANK VOLLMER¹

¹*Living Systems Institute, University of Exeter, Stocker Road, Exeter, EX4 4QD, UK*

²*Currently with SeNSE, Indian Institute of Technology Delhi, Hauz Khas, New Delhi, India*

³*School of Mathematical and Physical Sciences, Faculty of Science, University of Technology Sydney, Ultimo, New South Wales, 2007, Australia*

⁴*ARC Centre of Excellence for Transformative Meta-Optical Systems (TMOS), Faculty of Science, University of Technology Sydney, Ultimo, New South Wales, 2007, Australia*

*cj403@exeter.ac.uk

This supplement published with Optica Publishing Group on 9 March 2023 by The Authors under the terms of the [Creative Commons Attribution 4.0 License](https://creativecommons.org/licenses/by/4.0/) in the format provided by the authors and unedited. Further distribution of this work must maintain attribution to the author(s) and the published article's title, journal citation, and DOI.

Supplement DOI: <https://doi.org/10.6084/m9.figshare.22154918>

Parent Article DOI: <https://doi.org/10.1364/OE.485216>

Time-dependent Mandel Q parameter analysis for a hexagonal boron nitride single photon source: Supplemental Document

CALLUM JONES,^{1,*} JOLLY XAVIER,^{1,2} SAMIR VARTABI KASHANIAN,¹ MINH NGUYEN,³ IGOR AHARONOVICH,^{3,4} AND FRANK VOLLMER¹

¹Living Systems Institute, University of Exeter, Stocker Road, Exeter, EX4 4QD, United Kingdom

²Currently with SeNSE, Indian Institute of Technology Delhi, Hauz Khas, New Delhi, Delhi, India

³School of Mathematical and Physical Sciences, Faculty of Science, University of Technology Sydney, Ultimo, New South Wales, 2007, Australia

⁴ARC Centre of Excellence for Transformative Meta-Optical Systems (TMOS), Faculty of Science University of Technology Sydney, Ultimo, New South Wales, 2007, Australia

*cj403@exeter.ac.uk

Supplemental Document.

© 2021 Optica Publishing Group under the terms of the [Optica Publishing Group Open Access Publishing Agreement](#)

1. Pulsed timestamp filter

A filter was applied to the pulsed timestamp data before analysing the $g^{(2)}(\tau)$ and $Q(T)$ functions. Using the trigger pulse output of the pulsed laser, the time delay between each photon detection and the previous trigger pulse was available for all our data. A histogram of the delay time after the trigger pulse is shown in Fig. S1. The filter was applied by keeping only the detections which arrive within a given time window after the trigger pulse; all filters begin from the peak of the pulse at 7 ns delay. The following describes the process of choosing the optimum filter settings to exclude background noise counts and measure $Q(T)$ due to single photon emission counts only.

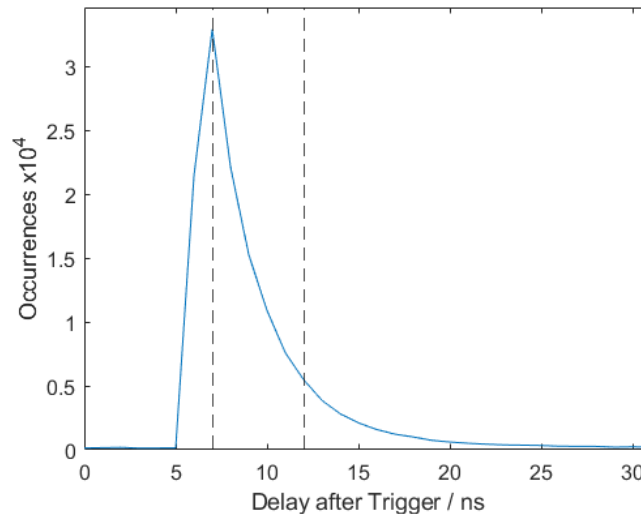


Fig.S1. Lifetime curve showing 5 ns filter width applied to the data.

The filter width was varied from 1 ns to applying no filter, i.e. using the raw data. The distribution of Q parameter values for $T = 100$ ns integration time over all 144 data

acquisitions is plotted as a function of filter width in Fig. S2. The raw data is plotted at 100 ns filter width as this corresponds to the pulse period, i.e. maximum possible filter width.

As the filter width goes to zero, $Q(T)$ also goes to zero since the number of counts being used for the calculation decreases.

Between 5 ns and 18 ns filter width there is a stable negative $Q(T)$. Above 18 ns however $Q(T)$ increases sharply and becomes positive. There is another increase above 80 ns filter width.

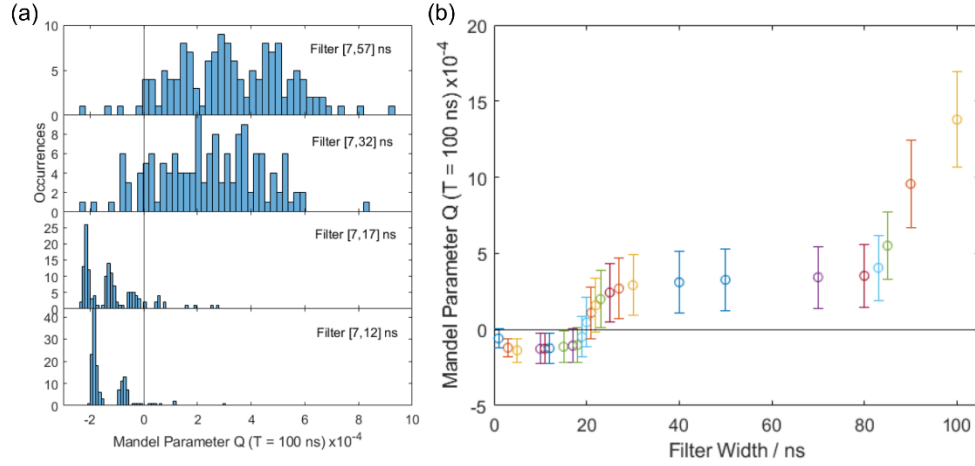


Fig.S2. (a) Mandel Q parameter at 100 ns integration time (integrating over one pulse period). Histograms show Q parameter values over the 144 data acquisitions each 100 s long, for different filter widths. (b) Mean Q parameter as a function of filter width.

The sudden increase in $Q(T)$ above 18 ns filter width can be attributed to an artefact of our measurement seen in the raw $g^{(2)}(\tau)$ data, see Fig. S3. There are additional peaks at ± 18 ns delay time in all $g^{(2)}(\tau)$ measurements. This only occurs when using multimode fibre to collect the output light from our setup, the delay time is always the same regardless of the light source being observed, and changing the length of multimode fibre at the output changes the delay time at which the peaks appear. Therefore we conclude these peaks are due to reflections from the end facets of our multimode fibre and as such we treat them as noise.

Using single mode fibres with angled (APC) connectors would solve this issue, however we use multimode fibre, which is widely used in other hBN experiments, in order to collect a high enough count rate under pulsed excitation to perform our measurements.

Note that for CW $g^{(2)}(\tau)$ measurements these peaks were still present, but since the peaks are narrow, they could be excluded from fitting procedures without significantly reducing the number of points used to fit models to the data.

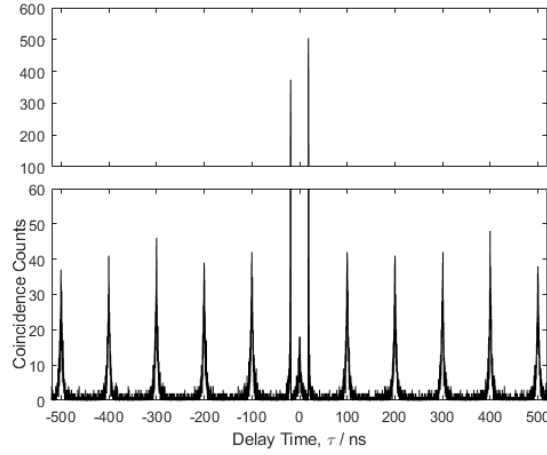


Fig.S3. Raw $g^{(2)}(\tau)$ function for pulsed excitation with 24 μW mean power showing noise peaks at ± 18 ns due to reflections in the multimode fibre.

The final choice of filter was 5 ns wide, i.e. over [7,12] ns delay time. This filter setting excludes the noise peaks at ± 18 ns in the $g^{(2)}(\tau)$ function while keeping enough photon counts to measure $Q(T)$ due to single photon counts from our hBN emitter. A 5 ns filter also produces the most significant negative Q value. This filter width is approximately double the radiative lifetime of the emitter: $\tau_{21} = 2.7 \pm 0.1$ ns.

We can also test the effect of applying a filter to the simulated pulsed timestamp data. In Fig. S4a we see that decreasing the filter width below ~ 5 ns moves $Q(T)$ closer to zero. Unlike the experimental data in Fig. S2b, $Q(T)$ does not change significantly for filter widths above ~ 5 ns because: a. the simulated data has no background noise, and b. the noise peaks at ± 18 ns delay are not present in the simulated data.

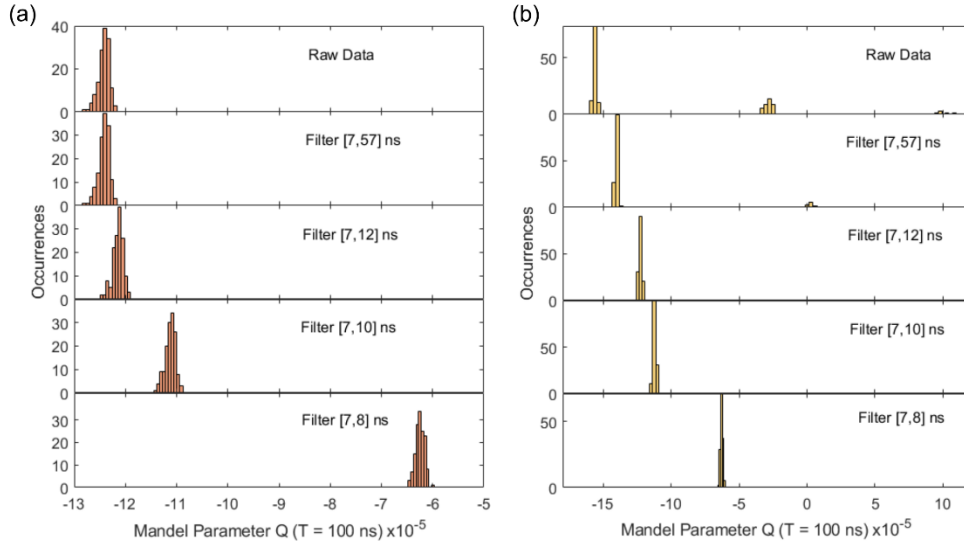


Fig.S4. Mandel Q parameter for simulated pulsed timestamp data at 100 ns integration time.
(a) Simulated Q parameter as a function of filter width. (b) Simulated Q parameter with uniformly distributed noise counts added to the simulated timestamp data.

One clear difference between the simulated and experimental $Q(T)$ histograms is that the simulation values are all clustered around a single value; the multiple peaks are only seen in

the experimental data. We added noise to the simulation by adding uniformly distributed background counts to the simulated timestamps, with the same background count rate of 160 ± 40 Hz per detection channel measured from experimental lifetime curves. With added noise, the simulated $Q(T)$ histograms in Fig. S4b do show multiple peaks and begin to resemble the experimental data more closely.

2. Detector deadtime measurement

The deadtime of our single photon avalanche diodes (SPADs) is nominally 77 ns. The deadtime must be known to choose an appropriate pulse repetition rate and to model the deadtime in Monte Carlo simulations. We measured the deadtime by detecting counts from room lights at around 4.4 MHz count rate, approaching the detector saturation count rate. The histogram of time delays between successive counts is shown in Fig. S5.

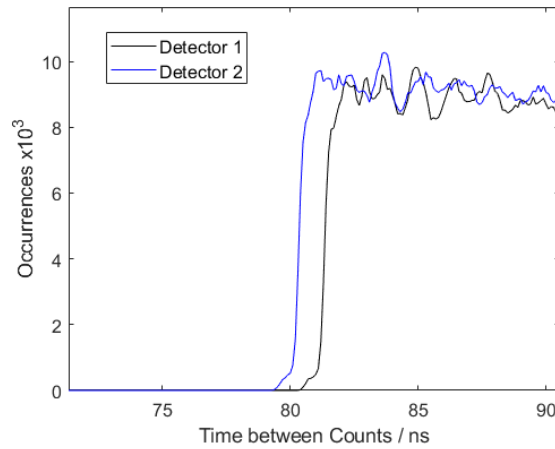


Fig.S5. Detector deadtime measurement using a near saturation count rate from room lights. Histogram of delay times between successive photon detections, showing a sudden drop to zero below the detector deadtime. Taking the deadtime as the half rise time of the curves, detector 1 deadtime $t_d = (81.35 \pm 0.10)$ ns; detector 2 deadtime $t_d = (80.35 \pm 0.10)$ ns. At high time delays the histogram slowly decreases to zero because we only consider nearest-neighbour delays.

The histograms show a sudden drop to zero for delays less than the deadtime. At large time delays the histograms slowly decrease to zero because we only accounted for the nearest-neighbour delays. Taking the deadtime to be the half-rise time of the curves gives values of $t_d = (81.35 \pm 0.10)$ ns for detector 1 and $t_d = (80.35 \pm 0.10)$ ns for detector 2. For the purposes of simulating timestamps we took the deadtime to be 80 ns for both detectors.

3. Detector afterpulsing

As well as a deadtime, SPADs can produce accidental electronic pulses after a photon detection. This artefact is known as afterpulsing.

Afterpulsing was characterised for our SPADs by measuring the histogram of delay times between trigger pulses and photon detections from the attenuated pulsed laser at 1 MHz repetition rate. Afterpulses are seen 80 ns after the pulse peak, and they decay with an exponential shape, see Fig. S6a. From this measurement the afterpulsing probability was determined to be 0.027, consistent with the datasheet value of <0.03 . A single exponential with 52 ns width was fitted to the afterpulse peak.

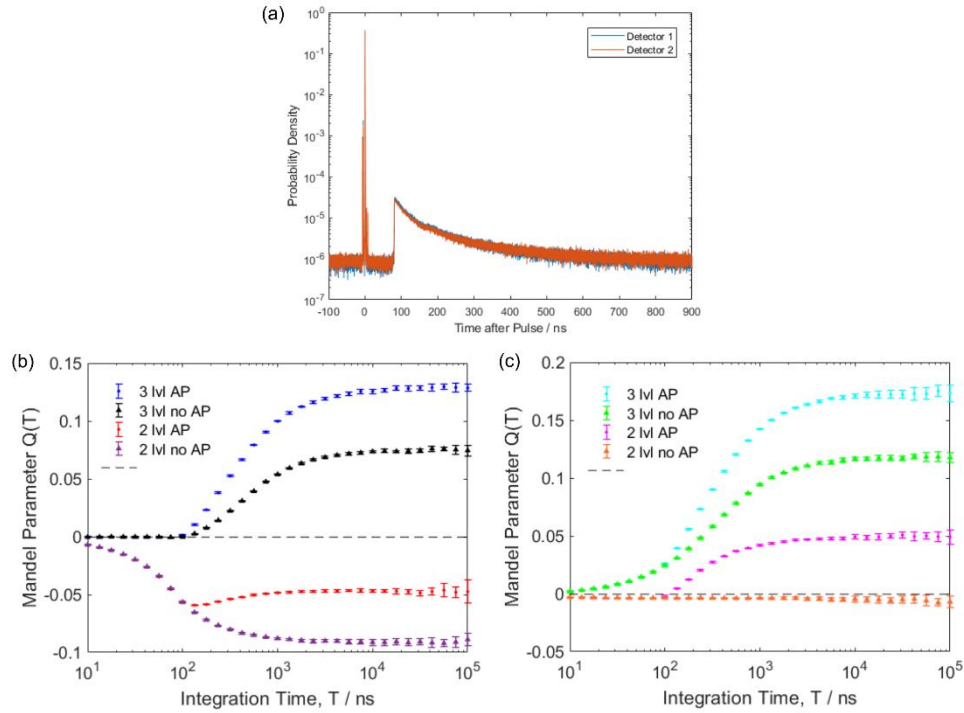


Fig.S6. Detector afterpulsing. (a) Measurement of delay histogram between trigger pulses and photon detections using an attenuated pulsed laser at 1 MHz. An exponential shaped afterpulse is seen one deadtime after the pulse peak. (b) Simulated CW Mandel Q parameter with 80 ns deadtime, showing the difference between including afterpulsing (AP) in the model for two- and three-level emitters (2 lvl, 3 lvl). (c) Simulated CW Q parameter with no deadtime, with and without afterpulsing. Afterpulsing was modelled with a probability of 0.027 and an exponential probability distribution starting at 80 ns with 50 ns width.

Afterpulses were also added to the Monte Carlo model for generating simulated timestamp data using the parameters we measured: an afterpulsing probability 0.027, and an exponential probability distribution starting 80 ns after detections with a width of 50 ns. The simulated data in Fig. 4b in the main text include these afterpulses. The effect of adding afterpulses is shown for two- and three-level emitters in Fig. S6b including the 80 ns detector deadtime, and Fig. S6c with no deadtime. In all cases afterpulsing causes more bunching in the $Q(T)$ function above 80 ns. However, it is still clear that a three-level system is required to describe the extent of the bunching seen in experiment (Fig. 4a in main text).

Due to the 5 ns filter applied to the pulsed timestamp data, most of the afterpulse counts are excluded from the $Q(T)$ calculation. Only counts close to 100 ns (the pulse repetition period) after the pulse will be included, since they ‘wrap around’ and arrive at the same time as the next pulse. We estimate this effectively reduces the afterpulsing probability to 0.0017, i.e. the afterpulsing effect is more than an order of magnitude smaller for the pulsed timestamp data than the CW data.

4. Pulsed $g^{(2)}$ as a function of power

Fig. S7 shows the $g^{(2)}(\tau)$ function under pulsed excitation as a function of the mean incident power, at 24 μW , 82 μW and 160 μW . The data had a 5 ns wide filter applied (over [7,12] ns delay after the trigger pulse). The value $g^{(2)}(0)$ was calculated as the ratio between the $\tau = 0$ peak area and the mean area of the 18 next nearest peaks, and the error was estimated as the

standard deviation of the peak areas. Values for $g^{(2)}(0)$ were: 0.37 ± 0.02 at $24 \mu\text{W}$, 0.69 ± 0.04 at $82 \mu\text{W}$, and 0.83 ± 0.06 at $160 \mu\text{W}$.

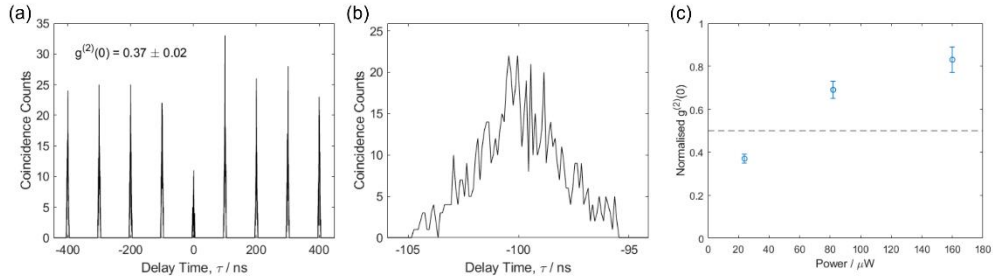


Fig.S7. (a) $g^{(2)}(\tau)$ under pulsed excitation at $24 \mu\text{W}$. The 5 ns width filter (over [7,12] ns delay after the trigger pulse) was applied to all timestamp data before calculating $g^{(2)}(\tau)$. (b) Zoom-in showing shape of $g^{(2)}(\tau)$ peaks after the filter was applied. (c) Power dependence of $g^{(2)}(0)$.

We found that under pulsed excitation the $g^{(2)}(0)$ value was very sensitive to power and the low power needed to achieve $g^{(2)}(0) < 0.5$ meant that the count rate had to be reduced significantly: the count rate was 2.8 kHz at $24 \mu\text{W}$ mean power.

The background count rate was measured from a single exponential fit to the $24 \mu\text{W}$ lifetime curve as 160 ± 40 Hz per detection channel (Fig. 2b in main text). This corresponds to only 0.04 coincidences per time bin in the $24 \mu\text{W}$ $g^{(2)}(\tau)$ histogram, therefore the background on the pulsed $g^{(2)}$ measurement was ignored. Note that the filtering process does remove background counts occurring outside the filter width.

5. Emitter spectral filtering

The output count rate as a function of tunable filter angle was converted into the spectrum in Fig. S8. The tunable filter bandwidth is around 20 nm. All measurements were done with the filter set to the maximum count rate at 595 nm (at 38° to optic axis).

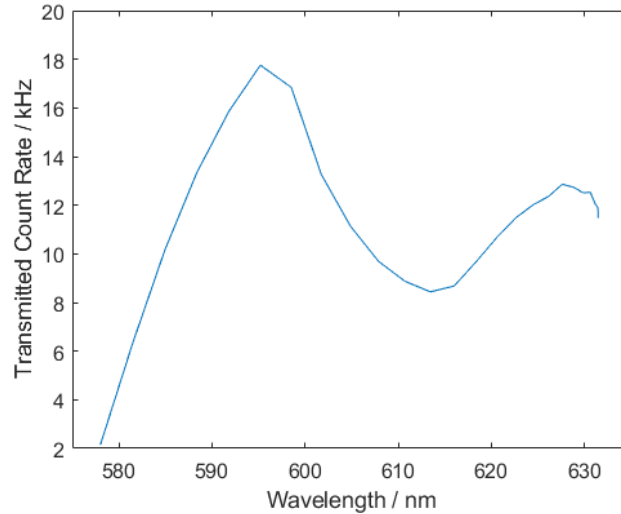


Fig.S8. Emission spectrum from our hBN emitter measured by rotating the angle tunable bandpass filter at the output. The bandpass filter has a bandwidth of around 20 nm. Peak emission count rate occurs at 595 nm, corresponding to a filter angle of 38° .

154 The significance of using spectral filtering is to improve the $g^{(2)}(0)$ value for our emitter:
 155 without the filter (filter completely removed from optical path) $g^{(2)}(0) = 0.56 \pm 0.10$, with
 156 the filter set to peak count rate $g^{(2)}(0) = 0.33 \pm 0.02$ (see Fig. 1c in main text).

157 6. Analytical solution for CW $Q(T)$

158 There is an analytical relation between $g^{(2)}(\tau)$ and $Q(T)$ in the continuous wave (CW) case,
 159 for integration time T and average photon count rate $\langle I \rangle$ this is given by [1, 2]:

$$160 \quad Q(T) = \frac{2\langle I \rangle}{T} \int_0^T d\tau \int_0^\tau d\tau' (g^{(2)}(\tau') - 1). \quad (S1)$$

161 We can calculate this for a $g^{(2)}(\tau)$ function which is well described by a two-exponential
 162 fit with lifetimes t_1, t_2 :
 163

$$164 \quad g^{(2)}(\tau') = 1 - (1 + a) \exp\left(-\frac{|\tau'|}{t_1}\right) + a \exp\left(-\frac{|\tau'|}{t_2}\right). \quad (S2)$$

165 For simplicity the bunching amplitude is described by one parameter a , so that $g^{(2)}(0) = 0$.
 166 Substituting into Eq. (S1):
 167

$$168 \quad Q(T) = \frac{2\langle I \rangle}{T} \int_0^T d\tau \int_0^\tau d\tau' \left(- (1 + a) \exp\left(-\frac{|\tau'|}{t_1}\right) + a \exp\left(-\frac{|\tau'|}{t_2}\right) \right)$$

$$169 \quad Q(T) = \frac{2\langle I \rangle}{T} \int_0^T d\tau \left(-t_1(1 + a) \left(1 - \exp\left(-\frac{\tau}{t_1}\right) \right) + t_2 a \left(1 - \exp\left(-\frac{\tau}{t_2}\right) \right) \right)$$

$$170 \quad Q(T) = \frac{2\langle I \rangle}{T} \left(t_1^2(1 + a) - t_2^2 a - (t_1(1 + a) - t_2 a)T - t_1^2(1 + a) \exp\left(-\frac{T}{t_1}\right) + t_2^2 a \exp\left(-\frac{T}{t_2}\right) \right). \quad (S3)$$

171 Here we have an analytical expression for the CW Mandel Q parameter for an ideal
 172 ($g^{(2)}(0) = 0$) single photon emitter including bunching.
 173

174 We can plot this function using values from CW $g^{(2)}(\tau)$ measurements under 250 μW
 175 excitation. In Fig. S9 the analytical $Q(T)$ expression is plotted for bunching parameter $a = 0.3$,
 176 antibunching and bunching times $t_1 = 2.7$ ns and $t_2 = 200$ ns, and single photon count rate
 177 $\langle I \rangle = 34$ kHz. Note that the count rate $\langle I \rangle$ already includes the total detection efficiency so
 178 accounts for losses in the optical path.

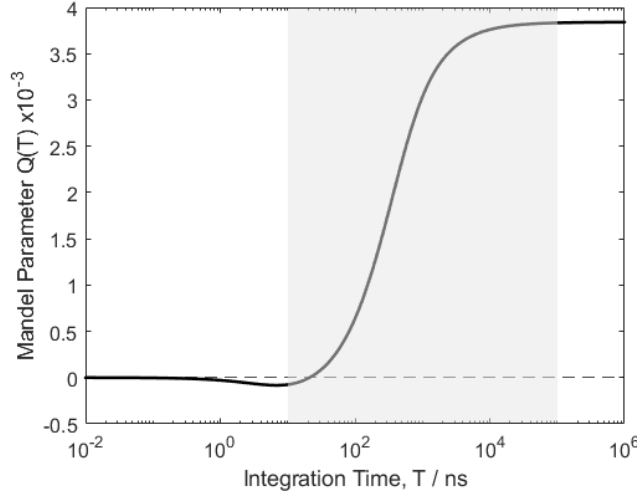


Fig.S9. Analytical solution for CW Mandel Q parameter. The function in Eq. (S3) was plotted with parameters $\alpha = 0.3$, $t_1 = 2.7$ ns, $t_2 = 200$ ns, and single photon count rate $\langle I \rangle = 34$ kHz. Shaded region shows the range plotted for experimental and simulated data in Fig. 4 of the main text.

The shaded region indicates the range plotted for experimental and simulated $Q(T)$ in Fig. 4 of the main text. The limiting behaviour at high and low T is the same as that in the experimental data; in particular $Q(T)$ tends to zero at low T . We also see that the crossover time from negative to positive $Q(T)$ occurs at around 21 ns, much lower than the 100 ns seen in the experimental data. The analytical model does not include all transition lifetimes of the three-level emitter τ_{ij} , or the effect of detector deadtime.

It would also be possible to produce an analytical solution for the pulsed Mandel Q parameter. However, this would be more challenging because the pulsed $g^{(2)}(\tau)$ histograms are noisier due to the relatively low photon count rate under pulsed excitation. As such there are fewer constraints when choosing a function to use in Eq. (S1), with parameters which model pulsed $g^{(2)}(\tau)$ well.

References

1. R. Short, and L. Mandel, "Observation of Sub-Poissonian Photon Statistics," Phys Rev Lett **51**, 384-387 (1983).
2. B. Lounis, and M. Orrit, "Single-photon sources," Rep. Prog. Phys. **68**, 1129-1179 (2005).